Reconstruction of tomographic images of dry aqueous foams

I.T. Davies[a,*], S.J. Cox[a], J. Lambert[b]

[a] *Institute of Mathematics and Physics, Aberystwyth University, Aberystwyth, Ceredigion SY23 3BZ, UK.*
[b] *Institute de Physique de Rennes, Université Rennes 1, 35042 Rennes Cedex, France.*

Abstract

X-ray tomography offers the possibility to examine the local changes in the structure of a three-dimensional aqueous foam as it flows, allowing a better fundamental understanding of foam rheology and the validation of models. We present an automated algorithm that reconstructs a dry aqueous foam from such images. Our algorithm uses ImageJ to extract from an image the topology of the network of Plateau borders in the foam, and then analyses this network to re-create the films and then the bubbles, and equilibrates the structure in Surface Evolver. We validate our algorithm and demonstrate its precision by applying it to simulated foam structures and analysing the topology and geometry obtained. We then apply our algorithm to a sequence of images from an experiment in which a spherical bead falls under its own weight through a polydisperse dry foam. This allows us to describe the evolution of the foam's liquid content and the bubble volumes with time as well as the distribution of bubble pressure and the forces exerted on a falling sphere.

Keywords: Reconstruction, dry foams, ImageJ, Surface Evolver, rheology.

1. Introduction

Aqueous foams are widely used in a number of processes, including ore separation and enhanced oil recovery. Their two-phase structure, consisting of gas bubbles in a liquid matrix, gives them many peculiar and useful properties, for example a yield stress [1, 2]. The liquid structure consists of a network of liquid-carrying channels called Plateau borders, which surround each thin film. Plateau's laws and the Young-Laplace law dictate that in an equilibrium dry foam (that is, one of low liquid content) the Plateau borders meet in fours at the tetrahedral angle, and the films are surfaces of constant mean curvature that meet three-fold at Plateau borders at 120° angles. To understand the interplay between foam structure and dynamics, mathematicians and physicists have often turned to two-dimensional systems [3] because of the ease with which they can be made, probed and modeled. Yet understanding the dynamics of three-dimensional foams is not only important, but continues to present unsolved problems.

The advent of synchrotron tomography and other non-destructive imaging techniques has led to unprecedented amounts of data about the internal structure of soft materials such as foams [4, 5], and even its evolution in time, provided that it does not evolve so quickly that it moves significantly while an image is being made. For foams, we now have access to sequences of images, containing thousands of bubbles, undergoing coarsening (bubble volumes evolve due to gas diffusion between them) [6, 7, 8, 9], drainage (liquid motion through the network of Plateau borders), and rheology (bulk motion of the foam itself) [10]. The significant drawback in all these imaging techniques is that they do not resolve the films between bubbles. That is, the images and videos obtained appear to be of *open-cell* foams, and it is necessary to somehow infer where the films are located from the shape and topology of the Plateau border network. Only then can the individual bubbles be reconstructed. We tackle this problem here.

In the dry limit, Monnereau and Vignes-Adler [7] imaged foams of a few tens of bubbles and showed that it is possible to identify each vertex where four Plateau borders meet, connect them via Plateau borders (or edges), insert films (or faces), identify individual bubbles, and then allow the vertices to move so as to satisfy Plateau's laws. The result is a true foam structure with bubble volumes close to those in the imaged

*Corresponding author. Email address: itd@aber.ac.uk

foam. Then bubble pressures and the statistics of each foam can be determined, and bubbles tracked from one image to the next to calculate their change in volume due to coarsening. We seek to automate this method, and apply it to much larger foams.

In a wet foam, with high liquid content, the bubbles are close to spheres and almost surrounded by liquid. In this case the problem of reconstructing the bubbles, at least to a good approximation, is rather different. For example, variations of the watershed algorithm can be used [4, 8, 9, 11, 12] to segment and label bubbles.

The static structure of a foam and Plateau's geometric laws are a consequence of the foam minimizing its surface energy, proportional to surface area, and constant bubble volumes. Surface Evolver [13] performs this minimization process given the topology of the foam, as performed by Monnereau and Vignes-Adler [7]. However they did not tackle the question of whether the bubble volumes inferred from the reconstruction are sufficiently accurate that they should be used in the minimization, or whether it is in fact the vertex positions that are most accurately recorded, and that these should be the fixed entities. Ideally, both pieces of information should be used. If the liquid content of a foam is non-zero, as is the case in most experiments, then the vertices are slightly swollen, and it becomes difficult to determine precisely their position. On the other hand, taking as a volume constraint the volume of the polyhedral cell with straight edges and flat films is a coarse approximation.

Many data-sets have been collected for liquid foams using X-ray tomography; they include static and coarsening foams [8, 9], and flowing foams moving through a constriction [10] and around a fixed sphere [14]. We choose to examine an experiment in which a small sphere falls through a foam under its own weight: not just because of its relevance to froth flotation [15], but because changes in sphere velocity are related to changes in foam structure. Further, this is a situation which we have simulated in 2D [16] and 3D, so that we hope that the experimental results can eventually validate our simulations in this regime where the origin of the forces on the sphere are well known.

We begin by describing the experiments used to generate images that we work with (§2.1), before explaining our methods for Plateau border network extraction (§2.2), identification of the bubble faces (§2.3) and of the bubbles themselves (§2.4). In §3 we validate our method against an image of a simulated foam, before analysing the experimental images in detail (§4), extracting the local liquid fraction, bubble pressures, and the forces exerted by the foam on the sphere.

2. Method

2.1. Experiment

In the experiment, a light plastic sphere of diameter 4mm and weight 54±2.7mg falls slowly under gravity through a polydisperse foam [4, 9] created from distilled water, 4% commercial dishwashing liquid (Dreft, Procter & Gamble) and traces of C_6F_{14} to suppress diffusion-driven coarsening. The foam is contained in a cylindrical tube with a diameter of 15mm and height 50mm. A 7.6mm vertical section of the container was imaged once per minute using a mixture of absorption and phase-constrast X-ray tomography. Each scan takes only 10s, ensuring that the motion of the sphere is negligible during the scan. More details of the imaging procedure can be found in [4]. Each image has dimensions 1024×1024×512 pixels and a resolution such that each pixel has size 14.9 microns, so that Plateau borders appear about 5 pixels across, and are thus shown clearly. We describe the centre of the sphere with Cartesian coordinates $(x_0,\ y_0,\ z_0)$, with z pointing vertically upwards, opposite to gravity.

The sphere is released into the foam and the cylinder is moved relative to the camera so that the sphere is at the centre of the image. The position of the cylinder is then fixed for the capture of 5 images, during which time the sphere falls towards the bottom of the imaged region. The cylinder is then moved upwards before repeating the procedure. The data inspected here is a sequence of 85 images spanning 110 minutes.

The sphere moves very slowly – of the order of 1.5 μm/s – and so we assume that the foam is at equilibrium in each image. Then the forces that the foam exerts on the sphere are due to the pressures in the bubbles and the surface tensions in the soap films that touch it [17, 18]. Clearly to obtain both components requires that we know where the soap films are, yet this is the piece of information lacking from the tomography. Hence the need for the automated algorithm to recreate them described below.

2.2. Liquid network identification

We use ImageJ [19, 20] to turn each experimental image into a dry foam skeleton. Firstly, we use a 3D median filter [21] with a $3 \times 3 \times 3$ voxel resolution to smooth the image. That is, each voxel is assigned the median intensity of itself and its 26 neighbours. We then obtain a binary image of the network of Plateau borders, choosing an appropriate threshold that balances the need for minimal noise and a fully connected liquid network. Note that manual user input is required to choose the threshold for one image of the sequence, and then this is applied to all images in the sequence.

At this stage, we have a binary image in which the liquid (the Plateau borders) and the solid (the sphere and container wall) all have unit intensity while the rest of the image (the gas) has zero intensity. To isolate the liquid we apply the *Remove Outliers* processing tool, a 2D selective median filtering tool that replaces a pixel's intensity by the median intensity of pixels within a user defined radius. Applying it on a binary image allows for removal of a small group of pixels with intensity one that are surrounded by large regions of pixels with intensity zero. We choose a radius large enough so that applying the tool on each slice results in the removal of pixels that belong to the foam's Plateau borders. We re-slice the image and apply the tool for all three coordinate directions. The resulting binary image now includes only the sphere and the container, which we then subtract from the initial binary image, creating a binary image of the liquid network (see figure 1a).

We approximate this network of Plateau borders as a skeletal network of straight edges as follows: (i) thinning the liquid structure using an algorithm implemented in the *Skeletonize3D* plug-in [22, 23] of ImageJ (see figure 1b); (ii) extracting the topology of the network using the *AnalyzeSkeleton* plug-in [24] to give the position of each vertex (i.e. voxels with more than two neighbours) and those vertices connected by an edge; (iii) re-structuring this information into a Surface Evolver [13] input file. An image of a network of straight edges obtained in this way is shown in figure 1c. Finally, to compensate for errors in the skeletonization at "swollen" wet vertices, we apply a correction by deleting very short edges. This leaves a structure with mostly 4-fold vertices, but that may include 6-fold and 8-fold vertices.

2.3. Face identification

Having imported the edge network into the Surface Evolver software [13], we use it as a tool to explore the topology of what is, in effect, a cyclic graph. The goal is to find all the irreducible cycles, as explained by [25], which are the faces, or soap films. We expect that most cycles will have lengths n between $n = 4$ and $n = 6$, since most faces in a disordered 3D foam are quadrilaterals, pentagons, or hexagons [26]. The procedure is as follows:

- All vertices and edges are labeled with a distinct number and each edge is given a direction, starting at the vertex with the lowest label.
- All paths consisting of $n = 3$ contiguous edges are found. If the start and end vertices are the same then this is a cycle. Each ordered cycle is stored as a new face. Plateau's laws imply that we need no longer consider edges that are part of three faces.
- We then generate all paths of length $n = 4$ in the same way, and continue to increment n until we reach a chosen upper limit of $n = 14$, at which stage we presume that all faces have been found.

Note that the cycles found are not necessarily planar. Thus to create a face, the Surface Evolver firstly positions a new vertex at the average position of the vertices in the cycle and then triangulates using this vertex.

This process is highly memory intensive, since it has to hold in memory many paths that are part of more than one face and may never be used. In practice, we have found that the time that the procedure takes is highly dependent on the number of bubbles in the image: using a desktop PC, it takes less than 30 minutes for images with approximately 250 bubbles, but over 12 hours for images with over 1000 bubbles. In its favour, it successfully identifies faces on the boundaries of the foam (either against the cylinder wall, or on the top and bottom image boundaries). It also copes with vertices connected to six or eight edges, rather than the four stipulated by Plateau's laws, which arise due to vertices swollen with liquid in the original image.

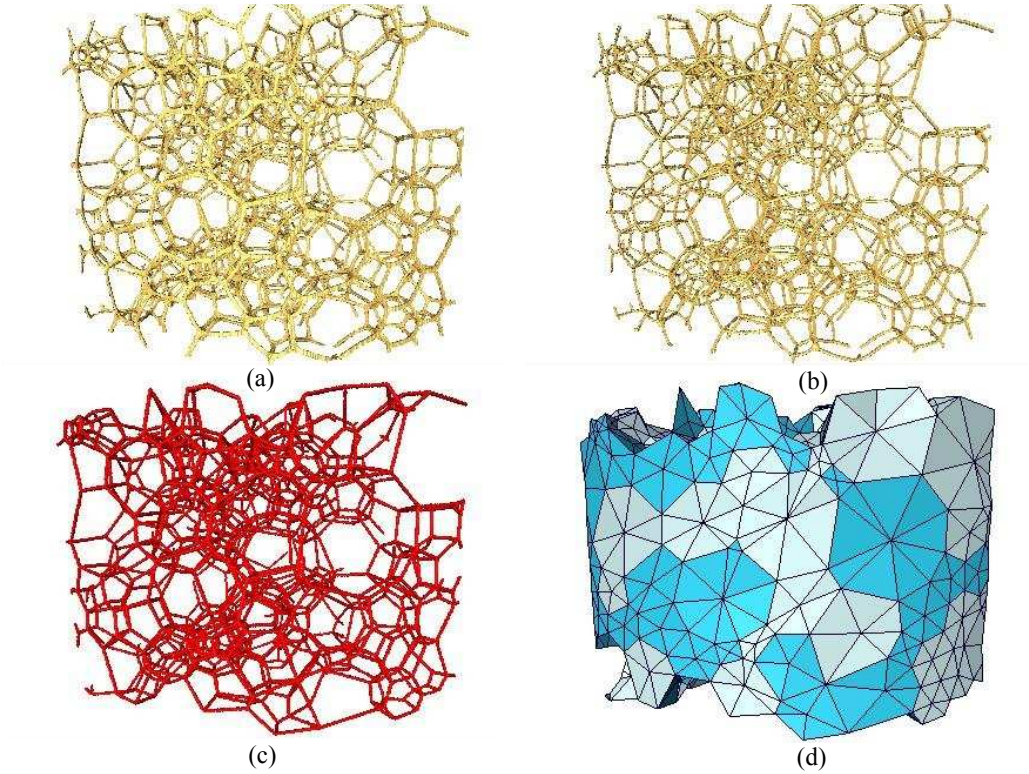

Figure 1: Steps in the reconstruction algorithm: (a) Isolate the network of Plateau borders by filtering. (b) Skeletonize this binary image. (c) Extract the topology of the Plateau border network. (d) Reconstruct the films by finding cycles in the cyclic graph defined by the skeleton and define bubbles as the enclosed cells of this structure.

2.4. Bubble identification

To find bubbles, we scan for regions enclosed by faces. We determine the faces belonging to bubble k with the following procedure:

1. Choose a face $f_{k,1}$ with the smallest ID label, the first face of the bubble k.
2. Scan for the nearest face in the normal direction to $f_{k,1}$. Denote this face by $f_{k,2}$, the second face of bubble k.
3. Define the point $P_{(k,centre)}$ as the midpoint of the segment joining the centres of faces $f_{k,1}$ and $f_{k,2}$; this is an approximation to the centre of the bubble k.
4. Find all other faces ($f_{k,i}$) of bubble k by checking whether each face that neighbours face $f_{k,1}$ or $f_{k,2}$ is the nearest to $P_{(k,centre)}$ along the line joining its centre to $P_{(k,centre)}$.
5. Update the position of $P_{(k,centre)}$ as the average of vertices of all faces that belong to bubble k.
6. Repeat steps (4) and (5) until the faces completely encloses a bubble. That is, until there are no remaining edges with one face belonging to the bubble.

The above procedure is repeated until all enclosed cells are found, that is until all internal faces are part of two bubbles and all external faces are part of one bubble. The time taken by this step of the algorithm is linearly dependent on the number of bubbles in the image; it takes about 20 minutes on a desktop PC to find 500 bubbles.

2.5. Foam structure and energy minimization

The final step in our algorithm is to minimize the surface area of the foam subject to imposed volume constraints on the bubbles. It is reasonable to assume that the foam is at equilibrium for every good quality image. Note that any motion of the foam during image acquisition, for example due to T1s, leads to very noisy and unusable images. Thus, we reconstruct a foam at equilibrium, that is, at a minimum of surface area subject to certain bubble volumes.

The bubble volumes are unknown, and so we must approximate them using information from the images. Our approach is to approximate the volume of each bubble by the volume enclosed by the triangulated surfaces determined by the bubble identification procedure (§2.4).

We then use the Surface Evolver to minimize the surface area of the foam. The software iteratively varies the position of the vertices while respecting these volume constraints, and we refine the edges and faces, ensuring that the triangular facets have a smaller area than 500 pixels, to allow them to curve. Edges and vertices at the top and bottom of the foam are kept fixed, since their position is determined by parts of the foam outside the image. An example of a reconstructed foam is shown in figure 2b.

3. Validation

To validate our reconstruction algorithm, we apply it to a dry foam structure simulated in Surface Evolver, that is, a foam in which the precise topology and the distributions of bubble volumes and pressures are known. We choose two test structures: a monodisperse foam and a polydisperse foam, each of 64 bubbles contained within a rigid spherical container (see figure 3a). This spherical outer boundary partly mimics the curved cylindrical outer wall in the experiments described above, but doesn't contain free boundaries, such as at the top and bottom of the experimental images, which are more difficult to deal with in a simulation.

We save all data from a converged simulation of the foam, in particular details of the topology of the liquid network and the geometry and pressure of each bubble. We then discard all this information by removing films and straightening the edges, to leave a network of straight edges, as for the analysed experimental images. We are then in a position to apply our reconstruction algorithm to identify the films and the bubbles and to re-equilibrate the foam. To compare, we match these bubbles with those in the simulation by correlating the position of the centres, defined as the average of the position of each bubble's vertices.

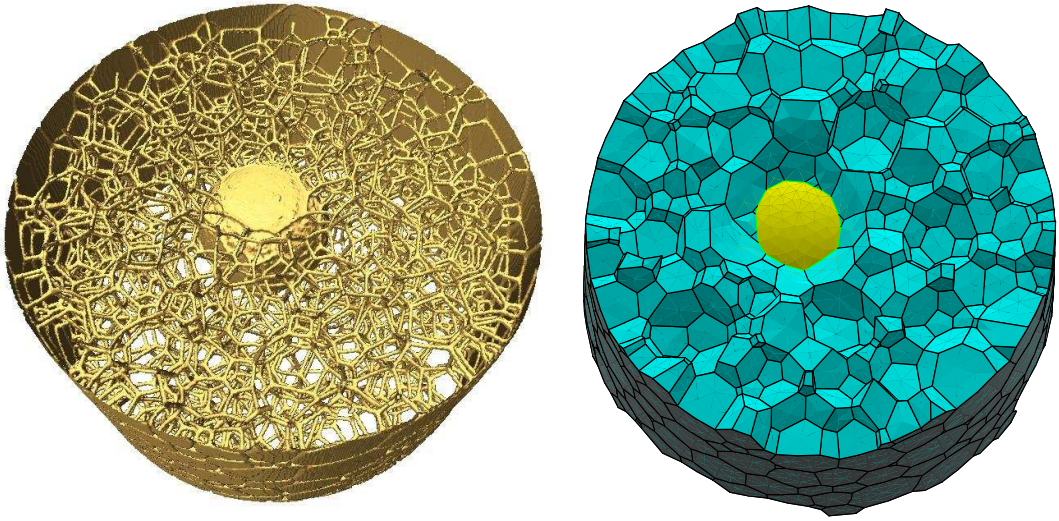

(a) (b)

Figure 2: A sphere immersed in a dry (liquid fraction $\phi_l \approx 1\%$) aqueous foam, showing (a) a smoothed, binary image and (b) the reconstructed foam in Surface Evolver.

Foam Sample		$\mu_2(F)$	$\mu_2(n)$
Monodisperse	Simulation	0.070361	0.025304
	Reconstruction	0.070361	0.025304
Polydisperse	Simulation	0.069997	0.025387
	Reconstruction	0.069997	0.025387

Table 1: Comparison of the topology of simulated and reconstructed dry monodisperse and polydisperse foams.

3.1. Topology of the simulated foam

A first measure of the accuracy of the reconstruction is obtained by comparing the topology of the simulated and reconstructed structures, for both the monodisperse and polydisperse foams, in terms of the second moments of the distributions of the number of faces per bubble, $\mu_2(F)$, and of the number of edges per bubble $\mu_2(n)$:

$$\begin{aligned} \mu_2(F) &= \left\langle \frac{(F - \langle F \rangle)^2}{\langle F \rangle^2} \right\rangle, \\ \mu_2(n) &= \left\langle \frac{(n - \langle n \rangle)^2}{\langle n \rangle^2} \right\rangle. \end{aligned} \tag{1}$$

We find that both $\mu_2(F)$ and $\mu_2(n)$ are exactly the same for each foam (see table 1). We also checked each bubble individually and found each to have exactly the same number of faces and edges in the simulated and reconstructed foams, for both volume dispersities. Thus, our algorithm accurately reconstructs the topology of a foam.

3.2. Geometry of the simulated foam

We compare the geometry of the simulated and reconstructed foams by determining the L_1 metric for the error in bubble volumes V_i, the surface area per bubble, A_i, and the edge length per bubble, L_i (cf. [27]):

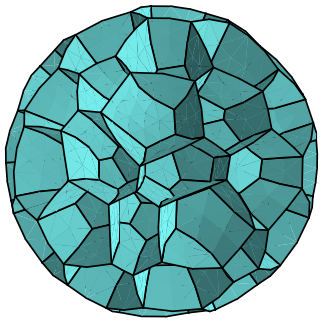

(a)

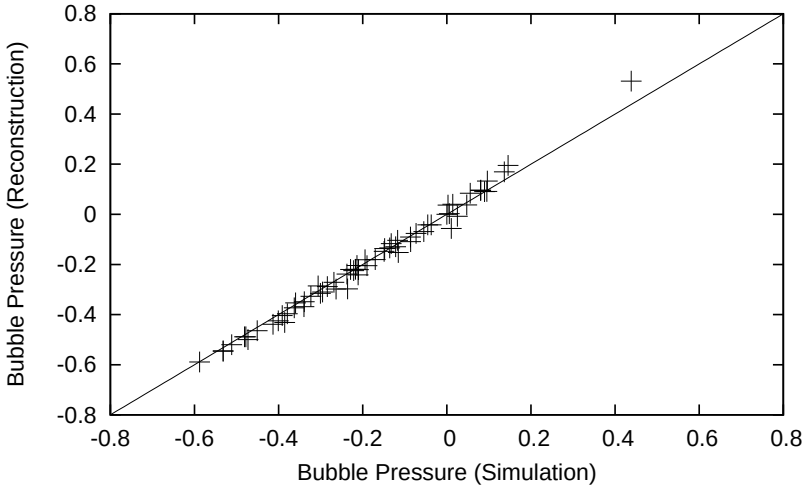

(b)

Figure 3: (a) The reconstruction algorithm is applied to this simulated monodisperse foam with $N = 64$ bubbles in a spherical container. The outer faces are removed. (b) Bubble pressures in the simulated and reconstructed foams, with correlation coefficients of $R = 0.998$ and $R = 0.976$ for the monodisperse and polydisperse foams respectively.

L_1 Error	Monodisperse	Polydisperse
$E(V)$	0.0424	0.0609
$E(A)$	0.0232	0.0254
$E(L)$	0.0105	0.0108

Table 2: L_1 error in the geometry of a foam reconstructed from a simulation, from eq. (2).

$$
\begin{aligned}
E(V) &= \frac{1}{V_{tot}} \sum_i^N \left| V_i^{rec} - V_i^{sim} \right| \\
E(A) &= \frac{1}{2A_{tot}} \sum_i^N \left| A_i^{rec} - A_i^{sim} \right| \\
E(L) &= \frac{1}{3L_{tot}} \sum_i^N \left| L_i^{rec} - L_i^{sim} \right|,
\end{aligned}
\tag{2}
$$

where the number of bubbles is $N = 64$ and V_{tot}, A_{tot} and L_{tot} denote the total volume, surface area and edge length of the simulated foam. Note that we only consider faces and edges that are not on the boundary of the sphere. Thus, each face separates two bubbles and each edge adjoins three bubbles, motivating the factors of 2 and 3 in the above equations.

For these foams, our approximation that bubble volumes are equal to those of the reconstructed volumes enclosed by triangulated surfaces (cf. §2.3 and 2.4) results in an error of up to 20% for an individual bubble (data not shown). However, the error in the L_1 metric for bubble volumes in the reconstruction is $5 \pm 1\%$ (see table 2). The precision of our algorithm in reconstructing the surface area and total edge length for each bubble is clearly demonstrated by the low values for $E(A)$ and $E(L)$ for the two foams tested (see table 2).

The last step of our algorithm, the equilibration in Surface Evolver, means that we are able to extract bubble pressures from images of foams. In figure 3b we show that we recover the bubble pressures of the simulated foam to high accuracy. The somewhat counter-intuitive result that the pressures are recovered

Network force	Simulation	Reconstruction
Mondodisperse foam	1.047	0.961
Polydisperse foam	1.721	1.766
Pressure force	Simulation	Reconstruction
Mondodisperse foam	1.152	0.862
Polydisperse foam	1.804	1.740

Table 3: The magnitude of the network and pressure forces exerted on the container. The network force acts inwards and the pressure force acts outwards; note that they are therefore almost equal and opposite in each case, as expected for a foam at equilibrium.

with higher accuracy than the volumes may be related to the observation that the growth rate of a bubble, which is proportional to the pressure, depends strongly on the number of faces [28, 29].

3.3. Forces on the container

A foam exerts a force on any solid surface that it touches. At equilibrium, this force has two components, as follows.

The network force, $\vec{F}^n$, is due to the pull of films in contact with the solid surface. It is given by the sum of the lengths of each edge (or Plateau border) in contact, multiplied by the surface tension γ, which is assumed constant here, resolved normal to the surface:

$$\vec{F}^n = \gamma \sum_{\text{edge, } i} l_i \vec{n}_i. \tag{3}$$

Here l_i denotes the length of edge i and n_i denotes the normal vector to the surface at the midpoint of that edge.

The pressure force $\vec{F}_p$, due to the pressure p_k of each bubble k in contact with the sphere, is given by

$$\vec{F}^p = \sum_{\text{bubble, } k} p_k \left(\sum_{\text{facet j}} a_j \vec{n}_j \right), \tag{4}$$

where a_j denotes the area of each facet of the triangulation of the surface of bubble k that contacts the sphere.

Since one of our goals is to be able to determine the drag on a sphere immersed in a foam, we test the ability of our algorithm to correctly reconstruct the forces acting on a solid surface by comparing the network force, $\vec{F}^n$, and pressure force, $\vec{F}^p$ exerted on the spherical container in the simulation and in the reconstruction. The magnitude of these forces is given in table 3.

The magnitude of the network force is found to high accuracy in both the monodisperse and the polydisperse foam, with a maximum error of 8%. The pressure force is less accurate, with an error of 25% for the monodisperse foam. This may be because the pressure force is very sensitive to the contact area of each bubble. Errors are smaller for the polydisperse foam. The direction in which the net forces act is also recovered accurately - we find an error of only 7° and 4° for the network force and 16° and 7° for the pressure force for the monodisperse and polydisperse foams respectively (data not shown).

4. Results

Having shown that the errors in our reconstruction algorithm appear to be modest, we now turn to the reconstruction of experimental images of real liquid foams.

4.1. Topology of the experimental foam

The topology of the foam can be described in terms of the distribution of the number of edges per face and the number of faces per bubble. In figure 4 we present the topology of a foam with 968 bubbles, which is close to the maximum number allowed by our reconstruction procedure, occurring after 30 minutes. We separate the data for the 315 peripheral bubbles (those touching the cylinder wall or the sphere) and those in the bulk.

The distribution of the number of edges per face, shown in figure 4a, peaks at five for bulk bubbles, but broadens for peripheral bubbles, a feature seen in Matzke's early experiments [30, 31] and found by Kraynik *et al.* [26] in simulations of highly polydisperse foams. That this foam is significantly polydisperse is confirmed by the distribution of the number of faces per bubble, F, which ranges from 4 to 28 (figure 4b). We find that $\langle F \rangle = 11.9$ and $\mu_2(F) = 0.16$ for bulk bubbles. There is again a slight downward shift between peripheral and bulk bubbles, although this is difficult to see because of the low number of bubbles in each class and hence the poor statistics. The peak for bulk bubbles is at 10, similar to a foam with polydispersity $p = 0.106$ in Kraynik *et al.*'s data [26]; this value of p corresponds to $\mu_2(F) \approx 0.15$, very close to our value. Note that there are many more bubbles with four faces (tetrahedra) than with five (triangular prisms).

4.2. Liquid fraction

We measure the amount of liquid in the foam both to obtain a vertical profile and a global average over time, based on a constant value of the threshold in the image analysis procedure described in §2.2 that gives the best rendering of the Plateau borders.

4.2.1. Liquid fraction profiles

The liquid fraction of each horizontal slice $\phi_l(z)$ of an image is given by the proportion of pixels inside the container in that slice with a binary value of one. From this information we obtain a profile of liquid fraction *versus* vertical position z in the container. Figure 5a shows that, as expected, the liquid content is lower at the top of the foam as a result of gravity-driven drainage [1] through the Plateau border network.

Note that every time that the cylinder is moved during the experiment, a different part of the foam is imaged so that it is not possible to compare the liquid fraction in a given part of the foam for the whole sequence of images. Nonetheless, it appears in figure 5a that the liquid fraction, and its gradient, both decrease in time at a given position.

4.2.2. Average liquid fraction

We use the *Voxel Counter* ImageJ plugin on each binary image to give the proportion of voxels with a binary value of one, and hence the average liquid fraction in the foam, $\langle \phi_l \rangle$. Figure 5b shows that $\langle \phi_l \rangle$ at first decreases with time and then reaches a plateau after roughly 30 minutes.

The reduction in the average liquid fraction is due to liquid drainage, and also perhaps to diffusion-driven coarsening. The latter is evident in the steady increase in the average bubble volume, shown in figure 5b, measured in the reconstructed foam. During the two hour experiment analysed in figure 5b, as many as three quarters of the bubbles eventually disappear, decreasing from approximately 1000 to 250 in this time.

4.3. Bubble pressure

We next describe the variation of bubble pressures in the experiment, relative to the position of the falling sphere. At equilibrium, the pressure in a bubble depends to a large extent on its volume (small bubbles have higher pressure) and also on its shape. In a rheological experiment such as this, we expect [32] bubbles situated directly below the sphere to be squeezed, and therefore to have high pressure while bubbles in the wake are stretched vertically and have lower pressure.

To visualize the bubble pressures, and to overcome the challenges and limitations of 3D visualizations, we reduce the data to 2D by averaging around a vertical line through the centre of the sphere. Thus in figure 6, we show the average bubble pressure (for a single experimental image) as a function of height z and distance r_s from this vertical line, so that each pixel (r_s, z) represents the average bubble pressure around a horizontal circular ring of radius r_s and centre (x_0, y_0, z).

Figure 6 shows a region of low pressure in the wake of the sphere, where a large bubble is positioned. A region of higher pressure lies next to the wake, which can be directly linked to an area of small bubbles

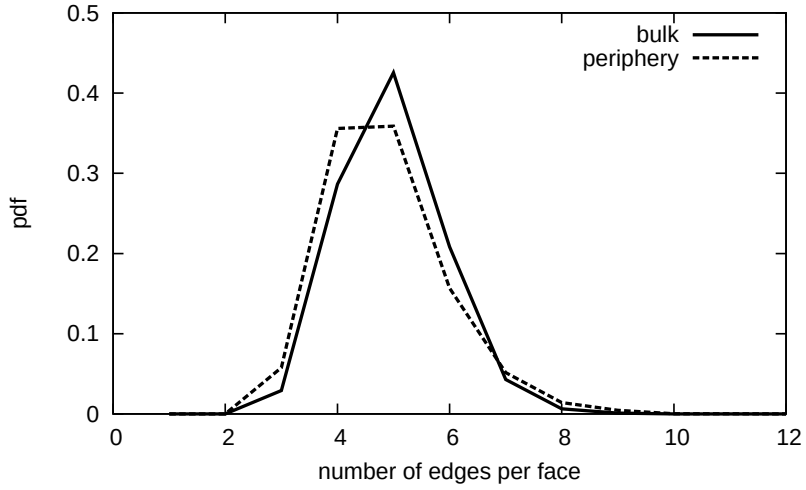

(a)

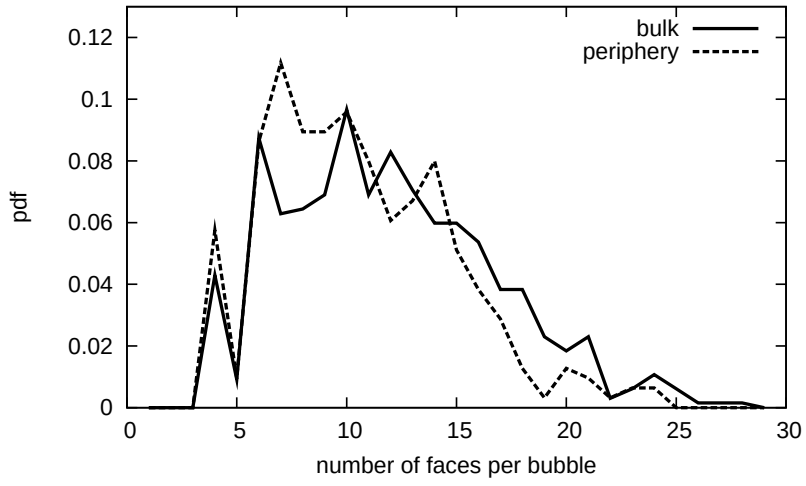

(b)

Figure 4: Statistical information for the foam's topology at a time of 30 minutes, separated into 653 bubbles in the bulk and 315 peripheral bubbles: (a) the number of edges per face, n, and (b) the number of faces per bubble, F.

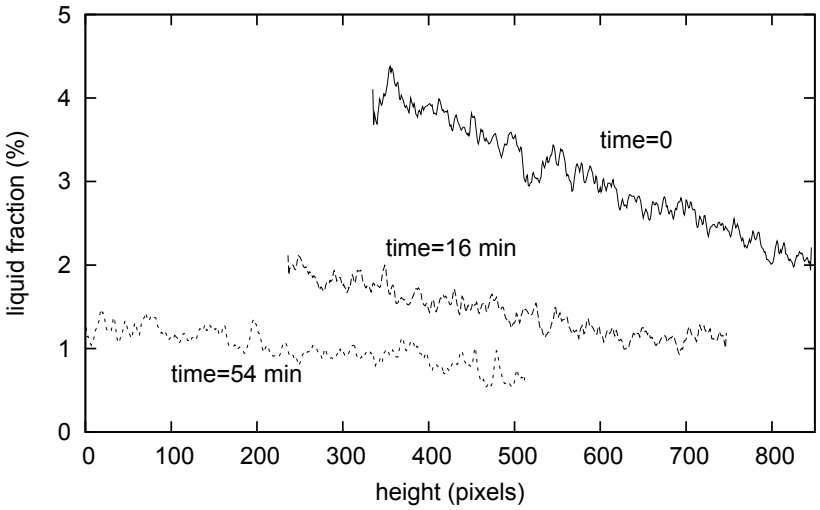

(a)

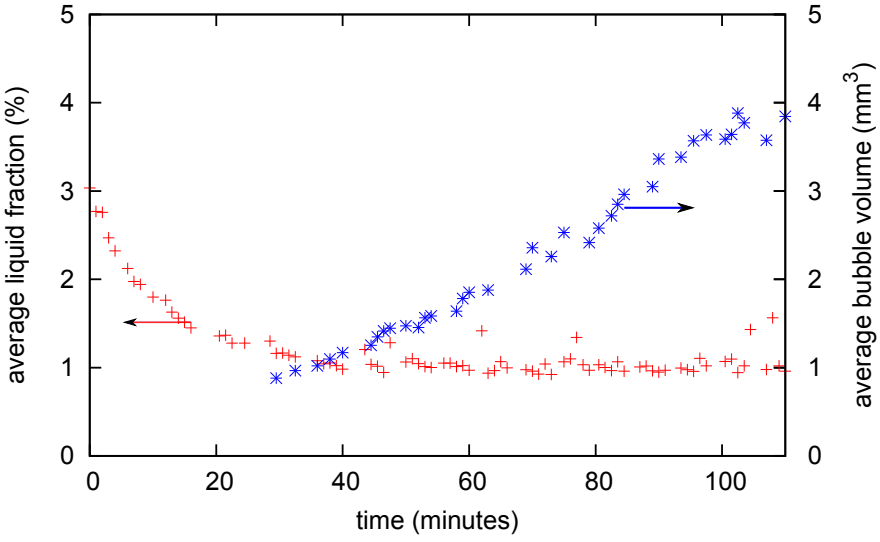

(b)

Figure 5: (a) Vertical profiles of liquid fraction in the experimental foam at three different times, showing that the foam gets drier. (b) The evolution of the average liquid fraction of the foam, $\langle \phi_l \rangle$, and average bubble volume, $\langle V_b \rangle$, *versus* time.

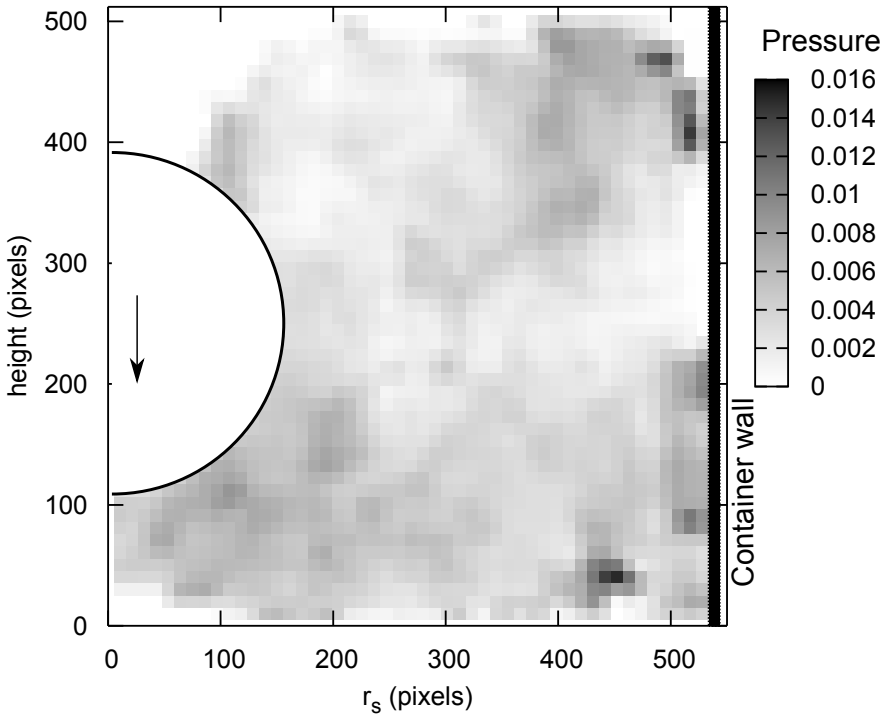

Figure 6: 2D visualization of bubble pressure for a single image of the foam at 50 minutes: Bubble pressure (with units $\gamma(\text{pixels})^{-1}$) is mapped over (r_s, z), where r_s denotes the radial distance from a vertical axis intersecting the sphere's centre and z denotes the height in the 3D image. The semi-circle shows the downward-moving sphere and the thick vertical line on the right represents the cylinder wall.

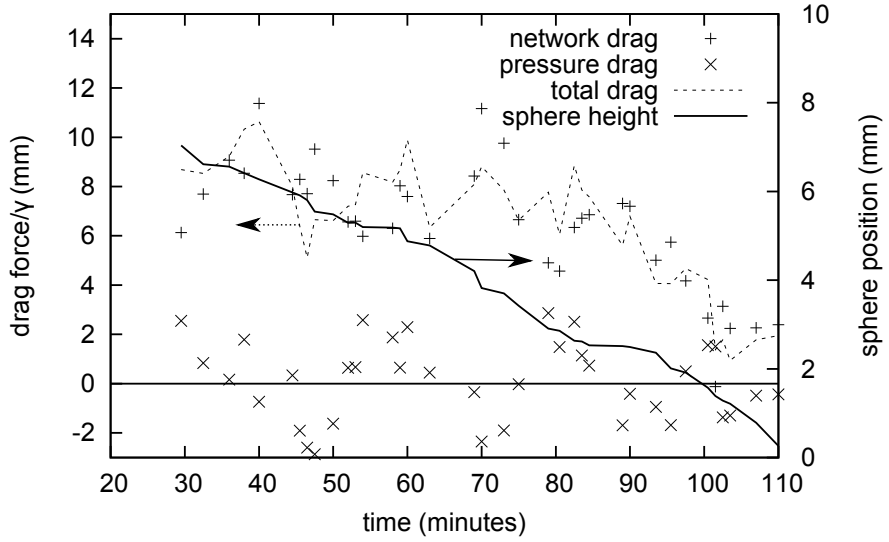

Figure 7: Variations in the network, pressure, total drag force on the sphere, shown alongside its vertical position, *versus* time.

touching the sphere. As expected, there is a region of higher pressure beneath the sphere where bubbles are squeezed. Regions of high pressure for large values of r_s correspond to highly deformed bubbles close to the cylinder wall.

4.4. Forces on the sphere

Our reconstruction of the full geometry of the foam allows us to calculate the forces on the sphere due to the liquid network and the pressures in the bubbles, as described in §3.3. (Note that, as in that section, since the reconstructed foam is at equilibrium, films contact surfaces at 90°; for the light, slow-moving sphere in the experiments considered here, this is a reasonable assumption.)

The components of these forces parallel to the z direction, that is the network and pressure drag, have significantly greater magnitude than the lift components, and we do not consider the latter any further. The variation of the network and pressure drag exerted on the sphere as it falls through the foam is shown in figure 7. The network force is the main contribution to the drag, by almost an order of magnitude. This agrees with 2D simulations [16, 32], which have also shown that the network force is greater than the pressure force. Using the results from figure 7, we can suggest an approximate value for the surface tension γ in the experiment. We consider the first 50 minutes shown in figure 7, where the downward motion of the sphere is approximately constant. Assuming that the network drag force ($F^n \approx 9\gamma$ mm) balances with the weight of the sphere over this period, we note that the surface tension is roughly $\gamma \approx 60 \times 10^{-3}\mathrm{Nm}^{-1}$, a reasonable value for water and commercial detergent.

One further feature of figure 7 is significant: both the pressure and network components of the drag force decrease with time. This is due either to the foam coarsening and the average bubble size increasing (figure 5b) or the sphere coming into contact with larger bubbles lower down in the foam. In consequence, the sphere's velocity increases during the experiment.

5. Summary

We have presented a detailed description of an algorithm to reconstruct three-dimensional dry aqueous foams, and have demonstrated its capability to extract precise information about the topology and geometry of a foam. We emphasize that the algorithm, in its current form, is designed to be applied to a *dry* foam, and it is computationally expensive compared to algorithms for wet foams, in which the bubbles are closer to spheres (see e.g. [12]). We validated the algorithm using simulated foams, showing that we recover bubble volumes and pressures to an accuracy of better than 20%. We applied the algorithm to a sequence

of experimental images of a sphere falling through a foam and presented preliminary results. It remains to extract more of the time-dependent features of the foam's behaviour, such as the fields of bubble displacement (velocity) and the local strain.

Acknowledgments

Funding from the British Council Alliance programme is gratefully acknowledged. ITD acknowledges funding from RIVIC and the Coleg Cymraeg Cenedlaethol. JL thanks Elhadji Mama Guène and Rajmund Mokso for providing experimental data. We also thank Francois Graner, Peter Cloetens and Andy Kraynik for stimulating discussions and Ken Brakke for developing and supporting the Surface Evolver.

References

[1] D. Weaire and S. Hutzler. *The Physics of Foams*. Oxford University Press, 2000.

[2] I. Cantat, S. Cohen-Addad, F. Elias, F. Graner, R. Höhler, O. Pitois, F. Rouyer, and A. Saint-Jalmes. *Les Mousses - Structure et Dynamique*. Belin, Paris, 2010.

[3] C.S. Smith. Grain shapes and other metallurgical applications of topology. In *Metal Interfaces*. American Society for Metals, Cleveland, OH, 1952.

[4] J. Lambert, I. Cantat, R. Delannay, A. Renault, F. Graner, J. A. Glazier, I. Veretennikov, and P. Cloetens. Extraction of relevant physical parameters from 3D images of foams obtained by X-ray tomography. *Coll. Surf. A*, 263:295–302, 2005.

[5] A.J. Meagher, M. Mukherjee, D. Weaire, S. Hutzler, J. Banhart, and F. Garcia-Moreno. Analysis of the internal structure of monodisperse liquid foams by X-ray tomography. *Soft Matter*, 7:9881, 2011.

[6] C. Monnereau and M. Vignes-Adler. Dynamics of 3D real foam coarsening. *Phys. Rev. Lett.*, 80:5228–5231, 1998.

[7] C. Monnereau, M. Vignes-Adler, and N. Pittet. Coarsening of a three-dimensional reconstructed foam under Surface Evolver. *Phil. Mag. B*, 79:1213–1222, 1999.

[8] J. Lambert, I. Cantat, R. Delannay, R. Mokso, P. Cloetens, J.A. Glazier., and F. Graner. Experimental growth law for bubbles in a moderately "wet" 3D liquid foam. *Phys. Rev. Lett.*, 99:058304, 2007.

[9] J. Lambert, R. Mokso, I. Cantat, P. Cloetens, J.A. Glazier., F. Graner, and R. Delannay. Coarsening foams robustly reach a self-similar growth regime. *Phys. Rev. Lett.*, 104:248304, 2010.

[10] S.A. Jones, B. Dollet, N. Slosse, Y. Jiang, S.J. Cox, and F. Graner. Two-dimensional constriction flows of foams. *Coll. Surf. A*, 382:18–23, 2011.

[11] N. Sadr-Kazemi and J.J. Cilliers. An image processing algorithm for measurement of flotation froth bubble size and shape distributions. *Minerals Engineering*, 10:1075-1083, 1997.

[12] K. Mader, R. Mokso, C. Raufaste, B. Dollet, S. Santucci, J. Lambert, and M. Stampanoni. Quantitative 3D characterization of cellular materials: Segmentation and morphology of foam. *Coll. Surf. A*. In press, 2013.

[13] K. Brakke. The Surface Evolver. *Exp. Math.*, 1:141–152, 1992.

[14] I. Cantat and O. Pitois. Stokes experiment in a liquid foam. *Phys. Fluids*, 18:083302, 2006.

[15] P. M. Ireland and G. J. Jameson. Drag force on a spherical particle moving through a foam: The role of wettability. *International Journal of Mineral Processing*, 103:78-88, 2012.

[16] I.T. Davies and S.J. Cox. Sedimenting discs in a two-dimensional foam. *Coll. Surf. A*, 344:8–14, 2009.

[17] B. Dollet, F. Elias, C. Quillet, C. Raufaste, M. Aubouy and F. Graner. Two-dimensional flow of foam around an obstacle: Force measurements. *Phys. Rev. E*, 71:031403, 2005.

[18] B. Dollet, F. Elias, C. Quilliet, A. Huillier, M. Aubouy and F. Graner. Two-dimensional flows of foam: Drag exerted on circular obstacles and dissipation. *Coll. Surf. A*, 263:101-110, 2005.

[19] M. D. Abramoff, P. J.Magalhaes, and S. J. Ram. Image processing with ImageJ. *Biophotonics International*, 11:36–42, 2004.

[20] W.S. Rasband. Imagej. *U.S. National Institutes of Health, Bethesda, Maryland, USA,*, http://rsb.info.nih.gov/ij/, 1997–2007.

[21] E. Iannuccelli, F. Mompart, J. Gellin, Y. Lahbib, M. Yerle, and T. Boudier. Nemo: A tool for analyzing gene and chromosome territory distributions from 3D-fish experiments. *Bioinformatics*, Jan. 14, 2010.

[22] T.-C. Lee and R.L. Kashyap. Building skeleton models via 3d medial surface/axis thinning algorithms. *CVGIP: Graphical Models and Image Processing*, 56:462–478, 1994.

[23] H. Homann. Implementation of a 3D thinning algorithm. *The Insight Journal*, December, 2007.

[24] I. A. Carreras, R. F. Gonzalez, A. M. Barrutia, and C. O. De-Solorzano. 3D reconstruction of histological sections: Application to mammary gland tissue. *Microscopy Research and Technique*, 73:1019–1029, 2010.

[25] F. Wooten. Structure, odd lines and topological entropy of disorder of amorphous silicon. *Acta Cryst. A*, 58:346–351, 2002.

[26] A. M. Kraynik, D. A. Reinelt, and F. van Swol. Structure of random foam. *Phys. Rev. Lett.*, 93:208301, 2004.

[27] S. D. Sintay and A. D. Rollett. Testing the accuracy of microstructure reconstruction in three dimensions using phantoms. *Modelling and Simulation in Materials Science and Engineering*, 20:075005, 2012.

[28] J. A. Glazier. Grain growth in three dimensions depends on grain topology. *Phys. Rev. Lett.*, 70, 2170-2173, 1993.

[29] S. Hilgenfeldt, A. M. Kraynik, S. A. Koehler and H. A. Stone. An Accurate von Neumanns Law for Three-dimensional Foams. *Phys. Rev. Lett.*, 86, 2685-2688, 2001.

[30] E. B. Matzke. The three-dimensional shape of bubbles in foam: An analysis of the role of surface forces in three-dimensional cell shape. *Am. J. Botany*, 33:58-80, 1946.

[31] E. B. Matzke and J. Nestler. Volume-Shape Relationships in Variant Foams. A Further Study of the Role of Surface Forces in Three-Dimensional Cell Shape Determination. *Am. J. Botany*, 33:130-144, 1946.

[32] C. Raufaste, B. Dollet, S. Cox, Y. Jiang, and F. Graner. Yield drag in a two-dimensional foam flow around a circular obstacle: Effect of liquid fraction. *Euro. Phys. J. E.*, 23:217–228, 2007.